

# Additive manufacturing innovations: Microstructure optimisation for ultra-high silicon electrical steel components

Rasoul Karami<sup>a,b,c,\*</sup>, David Butler<sup>d</sup>, Yashar Javadi<sup>a,e</sup>, Saeed Tamimi<sup>a,b,c</sup>

<sup>a</sup> Department of Design, Manufacturing and Engineering Management, University of Strathclyde, Glasgow, United Kingdom

<sup>b</sup> Advanced Forming Research Centre (AFRC), University of Strathclyde, Glasgow, United Kingdom

<sup>c</sup> National Manufacturing Institute Scotland (NMIS), University of Strathclyde, Glasgow, United Kingdom

<sup>d</sup> School of Engineering, University of Birmingham, Birmingham, United Kingdom

<sup>e</sup> Department of Electronics and Electrical Engineering, University of Strathclyde, Glasgow, United Kingdom

## ARTICLE INFO

### Keywords:

Additive manufacturing  
Non-grain oriented electrical steel  
Laser metal deposition  
Microstructure  
Crystallographic texture

## ABSTRACT

The main objective of this work is to fabricate high-silicon electrical steel with an optimized microstructure for magnetic applications through additive manufacturing (AM) routes. Traditional thermomechanical manufacturing routes, such as hot and cold rolling operations, have struggled to produce non-oriented electrical steel (NGOES) components with more than 3.4 wt% Si contents. However, the need for efficiency improvements requires an increase in silicon contents up to 6.5 wt%, leading to compromised magnetic and mechanical properties through conventional manufacturing techniques resulting in technical limitations on the production of these alloys. AM is a promising manufacturing approach that can address this challenge through near-net-shape fabrication. Optimisation process conditions in AM provide flexibility and enable better, more precise control over the microstructure. This study explores the microstructure and texture development of FeSi 6.5 wt% NGOES fabricated via laser metal deposition (LMD), with a build plate preheated to 200 °C to mitigate thermal stresses and cracking. The influence of process parameters on microstructure has been investigated. Process parameters, including laser power (400–500 W) and scanning speed, were adjusted to modify melt pool geometry, with energy density ranging from 74 J/mm<sup>2</sup> upward. Microstructure and texture were characterized using electron back-scatter diffraction (EBSD), revealing elongated grains with a strong <001>/BD fibre texture. Higher laser energy density enhances cube texture, improving magnetic properties, while increased laser power increases grain size, favouring <001> texture. These findings highlight the critical roles of energy density, laser power, and build plate temperature in tailoring NGOES microstructure and texture for enhanced performance.

## 1. Introduction

Non-oriented grain electrical steel (NGOE) finds primary application as core material in various fields, including transformers, generators, and electric motors. This preference is due to its significant magnetic properties, including high permeability, saturation magnetization, low core loss, and cost-effectiveness [1]. For decades, ongoing research efforts have focused on enhancing the magnetic properties of NGOES through texture development. However, using conventional and traditional methods for optimising texture through cold rolling and annealing treatment were usually exhibiting a hard magnetic direction such as <111> known as ( $\gamma$ ) and <110> known as ( $\alpha$ ) fibres, which is not desirable

for magnetic properties. To improve the magnetic performance of NGOES, the desirable texture such as <001> ( $\theta$ -fibre) known as an easy magnetic direction is required [1]. On the other side, NGOES with a high silicon content up to 6.5 % demonstrate improved magnetic properties, including enhanced electrical resistivity and reduced magnetic anisotropy. These characteristics are desirable for improving the efficiency of electric motors in electric vehicles. However, increasing Si content in NGOES lowers magnetic induction [2], creating a trade-off with desirable properties like reduced core losses. Additionally, it impairs sheet formability by promoting the formation of brittle intermetallic phases, B<sub>2</sub> and DO<sub>3</sub> which poses significant challenges for manufacturing these alloys using conventional methods [3] [4]. Furthermore, research from

This article is part of a Special issue entitled: 'ICOTOM' published in Materials Characterization.

\* Corresponding author at: University of Strathclyde, 16 Richmond Street, Glasgow, Scotland, United Kingdom.

E-mail addresses: [rasoul.karami@strath.ac.uk](mailto:rasoul.karami@strath.ac.uk) (R. Karami), [d.i.butler@bham.ac.uk](mailto:d.i.butler@bham.ac.uk) (D. Butler), [yashar.javadi@strath.ac.uk](mailto:yashar.javadi@strath.ac.uk) (Y. Javadi), [saeed.tamimi@strath.ac.uk](mailto:saeed.tamimi@strath.ac.uk) (S. Tamimi).

<https://doi.org/10.1016/j.matchar.2025.115002>

Received 27 November 2024; Received in revised form 28 March 2025; Accepted 31 March 2025

Available online 8 April 2025

1044-5803/© 2025 The Authors. Published by Elsevier Inc. This is an open access article under the CC BY license (<http://creativecommons.org/licenses/by/4.0/>).

nearly two decades ago demonstrated that columnar-type microstructures in medium- or low-Si NGOES electrical steels can exhibit favourable textures, such as theta-fibre components, which enhance magnetic performance. Despite these findings, producing such microstructures under industrial conditions remains a significant challenge [1].

To address all these points, additive manufacturing (AM) provides numerous advantages. These include design freedom [5], material flexibility, enhances sustainability by reducing material waste and energy consumption [6], precise control over processing parameters, and high solidification rate, all of which facilitate the desired microstructure and texture properties while minimising the occurrence of such phases in NGOES. Extensive research has explored AM's impact on FeSi alloys, with studies like Garibaldi et al. demonstrating how laser-based AM can achieve tailored columnar microstructures in high-silicon steels, and Backes et al. providing a comprehensive overview of microstructure evolution and magnetic properties in additively manufactured FeSi alloys. As demonstrated in a prior study [7] parts with a composition of 6.9 wt% FeSi were manufactured using selective laser melting, resulting in the absence of these phases. This result showed that, the rapid cooling rates during selective laser melting (SLM) processing, which suppress the formation of  $B_2$  and  $DO_3$  ordered phases, promoting a single ferritic phase. Consequently, a  $\langle 001 \rangle$  fibre-texture forms along the build direction (BD), transitioning to a cube-texture with increased laser energy due to altered melt-pool dynamics. This  $\langle 001 \rangle$  orientation, an easy axis of magnetization, underscores SLM's potential for producing grain-oriented high-silicon steels. However, elevating the laser energy also leads to greater crack formation and the development of spherical porosities [7].

Recent studies [8] demonstrate that Fe—Si alloys with up to 9 wt% silicon, processed via laser powder bed fusion (LPBF), exhibit high density but increased crack susceptibility at lower platform temperatures, becoming crack-free at 800 °C. These yields reduced core losses (e.g., 12 W/kg at 1 T compared to 21 W/kg for 3 wt% Si), enhancing energy efficiency for sustainable electrical applications. In contrast, our research [4] shows that preheating above 200 °C during LMD produces crack-free Fe—Si components (6.5 wt% Si) with optimized microstructure and  $\langle 001 \rangle$  texture, improving both energy efficiency and process feasibility.

A uniform columnar grain shape in the BD is highly desirable for FeSi, particularly for enhancing magnetic properties and texture along the  $\langle 001 \rangle$  direction [1], as well as for promoting Goss texture where the grains align with the magnetic flux directions [9]. This is confirmed by findings indicating that PBF-LB produces a checkerboard-like microstructure with elongated grains along the BD, where magnetic domains align with  $\langle 100 \rangle$  directions, potentially tailoring magnetic performance.

There is considerable debate about the optimal average grain size for improving the microstructure and texture of electrical steel, with proposed ranges varying widely: 50–150  $\mu\text{m}$  [10], 150  $\mu\text{m}$  [11] [12], 220  $\mu\text{m}$  [13], and even 536–615  $\mu\text{m}$  [14]. However, significant uncertainty persists regarding the relationship between grain size and magnetic properties. As noted, no clear correlation exists, since it is challenging to isolate grain size effects by developing microstructures with varying grain sizes but identical textures. Notably, magnetic induction depends directly on magneto-crystalline anisotropy energy density, further complicating this relationship [15].

The magnetic performance of electrical steel, such as hysteresis losses and permeability, relies on surface quality, which influences magnetic domain wall motion—vital for energy efficiency in transformers and electric motors [1]. In LMD, surface irregularities like roughness or cracks form due to rapid solidification [4], unlike the smoother surfaces of conventional methods like asymmetric rolling (ASR), which can enhance domain wall mobility through favourable textures (e.g.,  $\langle 001 \rangle // \text{ND}$ ) but may introduce defects like edge cracks and friction-induced roughness, increasing hysteresis losses and roller wear costs [1]. Coatings and techniques like resin infiltration in AM of Fe-6.5 wt%Si can

reduce losses and improve properties [16], yet LMD's surface challenges may increase core losses compared to traditional processes [17,18]. To address this challenge, various methods like physical vapor deposition (PVD) [19] and chemical vapor deposition (CVD) [20] can be employed which out scope of this paper. This study investigates the potential of LMD for electrical steel, emphasizing how processing parameters influence microstructure and texture evolution, which significantly affect magnetic properties; however, the specific effects on domain wall dynamics and optimisation strategies require further research.

In addition to that, the microstructure and crystallographic texture of FeSi still require improvement to reduce core losses and enhance the magnetic permeability of NGOES thin sheets. A uniform columnar grain shape in the BD is desirable for FeSi, particularly for enhancing magnetic properties and texture along the  $\langle 001 \rangle$  direction and Goss texture where the grains aligned with the magnetic flux directions. This alignment enables the orientation of magnetic moments in the BD, thereby maximising saturation magnetisation. Additionally, it makes FeSi more responsive to magnetic fields in the BD and reduces hysteresis losses when grains are aligned in the BD, as the majority of domains are already aligned with the applied field direction, consequently reducing the energy required for alignment [21,22]. Moreover, magnetic permeability is enhanced in the BD due to the alignment of grains, making it easier for FeSi materials to be magnetized by an applied magnetic field [23]. It has been reported that alternative AM processes such as LMD Al—Mg alloy [24], Ti—6Al—4 V [25], stainless steel 316 L [26] offer a distinct advantage in the development of columnar grains aligned with the BD. This is attributed to significant thermal gradients and solidification behaviours during the process, which promote rapid nucleation, grain growth, and directional solidification. When higher energy input is applied, these conditions favour the formation of columnar grains aligned with the BD. Such grain structures have the potential to enhance magnetic properties and promote a favourable texture in NGOES sheets, as evidenced by studies showing high-silicon Fe—Si alloys benefiting from AM's ability to control grain size and phase formation. Hence, this study seeks to investigate how the LMD process contributes to the development of the desired microstructure and crystallographic texture in high-silicon electrical steel. Evaluation of the microstructure and texture evolution utilizes optical and electron microscopies. Furthermore, the study examines the influence of LMD processing parameters, including laser power, scanning speed, and energy density, on the formation of the microstructure and texture.

## 2. Materials and experimental procedure

### 2.1. Sample processing

All samples in this study were manufactured from high silicon electrical steel gas-atomised powder (FeSi 6.5 wt%) with a size range of 45–110  $\mu\text{m}$  with a mean particle size of 77.5  $\mu\text{m}$ , a Hall flowmeter measurement of 19.0 s/50 g, and an apparent density of 4.06 g/cm<sup>3</sup> supplied by MSE Supplies LLC company. The chemical composition of NGOES used in this study is shown in the Table 1.

Hybrid LMD technologies were utilised, incorporating a 3 + 2 axis CNC Milling machine, a 1.5 kW Ytterbium Fibre laser, and localised argon shielding from a nozzle. In this investigation, only localised shielding was employed for depositing thin walls measuring 20 \* 30 \* 1.5 mm<sup>3</sup> to examine microstructure and crystallographic texture. A 1 mm spot size and a powder feed rate of 2.5 g/min were maintained for all depositions. The spacing between scan track centrelines within each layer, referred to as tracking space or hatch space for foundation layers, was set at 0.6 mm horizontally, while the vertical distance or thickness between each layer, known as z-step along the BD, remained fixed at 0.45 mm. The samples were processed with a variety of processing parameters such as laser power (P:400 to 500 W), constant scan speed (V:400 mm/min), energy density (E:60 to 75 J/mm<sup>2</sup>), as presented in the Table 2. The X axis is also referred to as the BD and samples were

**Table 1**  
Fe-6.5 wt%Si powder details.

Chemical composition (wt%)							Size distribution ( $\mu\text{m}$ )		
Fe	Si	Al	C	S	O	N	D10	D50	D90
92.90 %	6.60 %	0.46 %	0.005 %	0.005 %	0.009 %	0.004 %	34.5	78.5	116

**Table 2**  
Processing parameters for different samples.

Sample	Laser power (w)	Scan speed (mm/min)	Energy density ( $\text{J}/\text{mm}^2$ )	Powder flow (g/min)	Laser diameter (mm)	Track spacing (mm)	Z step (mm)
TW1	400	400	60	2.5	1	0.6	0.45
TW2	465	400	69.75	2.5	1	0.6	0.45
TW3	500	400	75	2.5	1	0.6	0.45

removed by wire electrical-discharge machining due to their size, precision cutting, and the minimal mechanical stress that can be achieved in this cutting process.

## 2.2. Sample preparation, optical microscopy and EBSD

Thin-wall samples, fabricated via LMD, were prepared for microstructural and crystallographic analysis through a series of steps. Samples were sectioned using an electrical discharge machining (EDM) system, followed by grinding with water-cooled SiC papers (grit sizes 240, 400, 800, 1200, and 2500) at a platen speed of 240 rpm and an applied force of 27 N for 3 min per step. Mechanical polishing was then conducted using a 3  $\mu\text{m}$  MgO oil-based Metadi suspension, followed by a final polish with Microcloth (both supplied by Buehler) at a platen speed of 150 rpm and a force of 27 N for 6 min. To achieve a surface suitable for optical microscopy, samples were etched with 2 % Nital (2 % nitric acid in ethanol). For EBSD analysis, optimal surface quality was further ensured by subjecting the samples to vibratory polishing for 30 min.

Microstructural features were examined using a 3D digital microscope (RH-2000, Hirox), while crystallographic texture was analysed via electron backscatter diffraction (EBSD) on the XY plane—defined as the plane where X corresponds to the build direction (BD) and Y to the normal direction (ND), with the scanning direction (SD) along the Z-axis aligning with the transverse direction (TD) and corresponds to the rolling direction (RD) in conventional terms—using Hirox and Leica microscopes for all samples. EBSD maps were collected with a step size of 3  $\mu\text{m}$  and the sample tilted 70° to the electron beam. The AZtec software was used to index FeSi 6.5 wt% based on  $\alpha$ -iron body-centered cubic (BCC) parameters, achieving an indexing rate exceeding 99 %. Texture analysis was performed using AZtec Crystal software, which processed EBSD maps covering the entire thin-wall cross-section to calculate orientation distribution functions (ODFs). The resulting inverse pole figure (IPF) maps, with texture type and strength varying across samples which will be shown in next sections.

## 3. Results and discussion

The primary aim of this study was to investigate how LMD processing parameters—such as laser power, scan speed, and energy density—affect the microstructure and crystallographic texture of high-silicon steel (6.5 wt% Si), with a focus on optimising grain orientation for enhanced material properties. The following discussion integrates experimental findings with literature to clarify the underlying relationships.

### 3.1. Microstructure evolution during LMD of FeSi 6.5 wt%

The microstructure of as-deposited LMD FeSi 6.5 wt% was examined to better understand the changes in microstructure that occur throughout the LMD process. As it can be seen in Fig. 1 microstructure

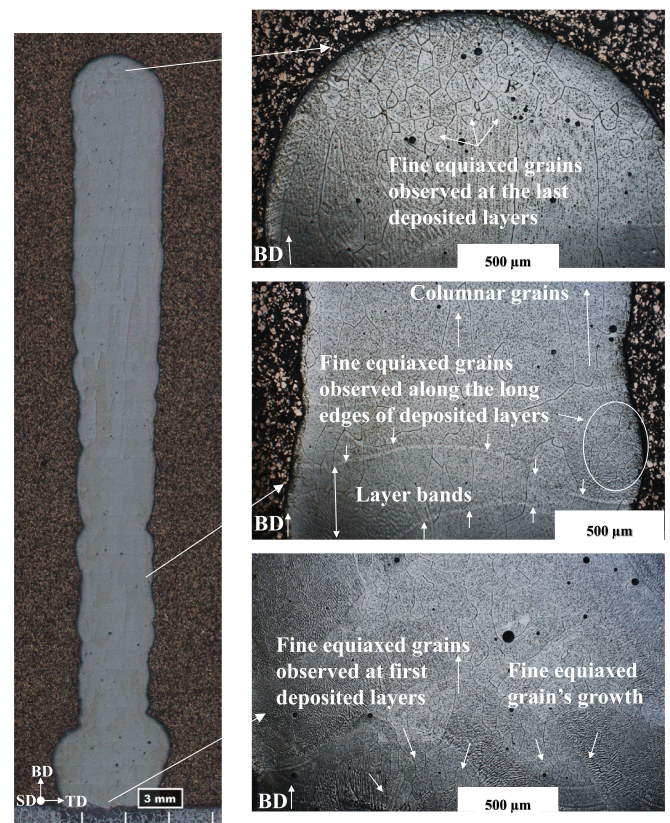


**Fig. 1.** The optical graph of etched specimen consisting of different sections of the sample.

consisted of columnar grains up to several millimetres in length aligned in the BD. However, fine equiaxed were observed after first, and last layers as well as some area in long edges of FeSi 6.5 wt% deposited. This behaviour is also observed in development of texture NGOES steel [27]. This observation is primarily due to a substantial temperature gradient within the melt pool, resulting in a rapid growth of columnar grains and decreasing the likelihood of new sites nucleating during the solidification process. Additionally, it can be observed that fine grains nucleated and formed at first layer, along the long edges, and at the last layer possibly due to the substrate acting as a thermal sink when the first layer of FeSi was deposited and being exposed to the atmosphere on both side (along edges) and three sides (top) of the samples cause to increase cooling rate and forming fine grains at these areas. This strategy exposes these areas to less laser time, resulting in lower heat accumulation due to the laser's travel time, thus promoting the development of new fine grains.

It is worth mentioning that optimising processing parameters such as appropriate laser power during the AM process can avoid defects such as keyholing and porosity at the bottom of melt pool [28]. It is desirable that to have melt pool in conduction mode with no defects such as entrapped gas porosity and keyholes. However, at high laser power, it is likely these types of defects will be present due to turbulence in the melt pool [29]. Characteristics of the melt pool such as thermal phenomena as well as heat transfer (conduction, convection, radiation) are key players in the stability of the melt pool during the additive manufacturing process [1,30]. The schematic of the thermal phenomena, melt boundary, and columnar grain development of FeSi 6.5 wt% during the LMD process can be seen in Fig. 2.

To investigate and understand the evolution behaviour of the microstructure during the layer-by-layer deposition process in the LMD process, an optical macrograph image has been obtained with the layer bands, as shown in Fig. 3. In this case, the melt pool size is notably large as observed in [31], primarily resulting from the high laser power's influence in the LMD process. This effect outweighs other factors such as feed rate and powder mass flow. Additionally, the melt pool size is further increased due to the preheating of the substrate. According to [32] preheating increases the depth of melt pool in the conduction area, leading to a deeper melt pool. Furthermore, as depicted in Fig. 1 and Fig. 3 numerous layer bands are observed, similar to the reported findings of [33,34]. This observation may be attributed to the superheating effect, which initiates melting in the previous layer's pool, forming a narrow band with a temperature exceeding the solidus temperature. However, due to limited time, the material remains in the solid phase. As can be seen in Fig. 3 the formation of a shallow melt pool with a curved surface occurs during the LMD process, where the melt pool is in motion. The solidification substructure primarily grows parallel to the BD due to the high thermal gradient, which is perpendicular to the melt pool. Notably, in this case, the melt pool tilts in the direction of the laser movement. This phenomenon has been reported by other researchers in more detail [35], and its impact on grain growth in the BD will be further explored in the EBSD case studies in section 3.2.

It is worth mentioning that defects such as pores can be detrimental for microstructure development. It is possible that pores can act as a thermal sink and absorb all heat provided by the laser not allowing the heat to distribute through the normal conduction across the sample and cause the temperature to rise in the melt pool Fig. 4. This abnormal temperature in the melt pool led to the formation of two different areas of equiaxed and elongated grains. At the tip of the pore, equiaxed grains

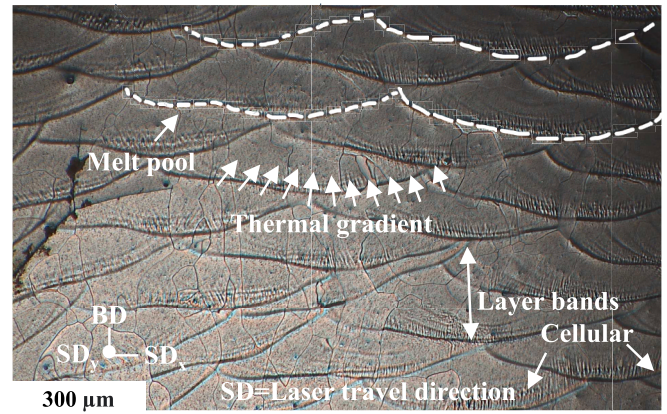


Fig. 3. Optical graph of the direction of maximum thermal gradient with respect to the melt pool geometry.

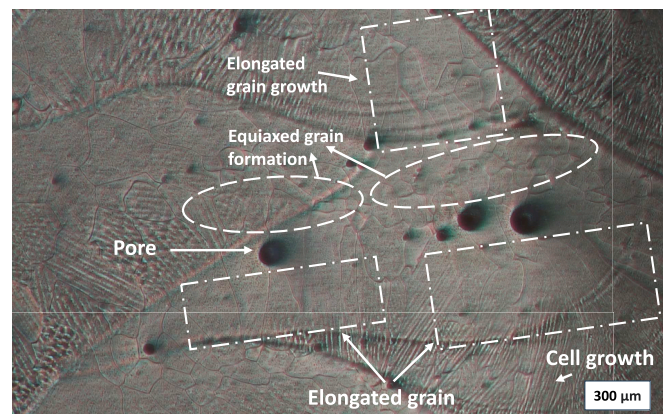


Fig. 4. Effect of pore on microstructural development.

form due to the presence of an air gap that blocks heat conduction distribution. This lack of a heat source and higher cooling rate contribute to the formation of smaller grains. Also, in the absence of defects, the above equiaxed grains, due to higher heat input, rapidly change in temperature across the sample, and directional solidification inherent in LMD, the grain starts to grow in specific direction and leading elongated grain structures. At the tip of the pore, the equiaxed grain is formed due to the existence of an airgap caused to block the heat conduction, distribution and due to lack of heat source and higher cooling rate which can lead to smaller grains. Also, in absent of defects, the above equiaxed grains due to higher heat input, rapid change in temperature across sample, and directional solidification inherent in LMD, the grain starts to grow in specific direction and leading elongated grain structures [36].

This phenomenon has also been observed in other additive manufacturing research, such as [7,26], where grains with a preferred crystal growth direction, such as  $\langle 001 \rangle$ , form along the building direction. These grains align closely with the thermal gradient direction, where rapid solidification occurs, while other grains with less favourable orientations are poorly aligned. In other words, the grains with  $\langle 001 \rangle$  direction aligned more closely to the vertical thermal gradient direction which is the BD and these preferred grains orientation grow and dominate, creating a columnar grain growing perpendicular to a surface in BD. Since epitaxial growth requires minimal undercooling to occur, cellular and columnar grains grow in an epitaxial manner from the substrate grain and creating a columnar grain growing perpendicular in the BD during directional solidification phenomenon Fig. 5 [37].

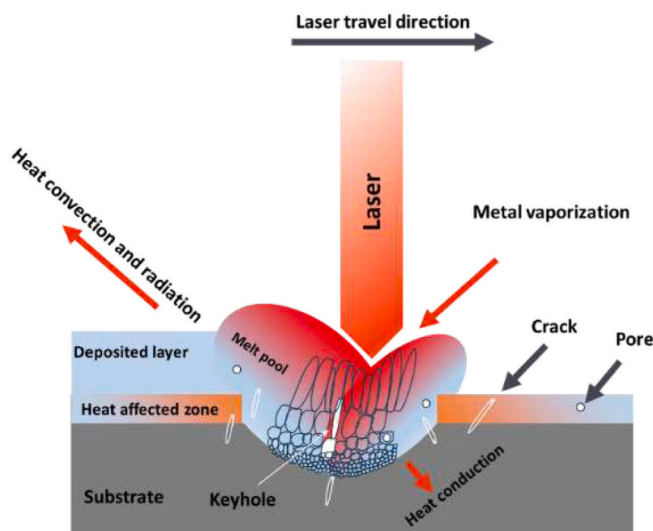
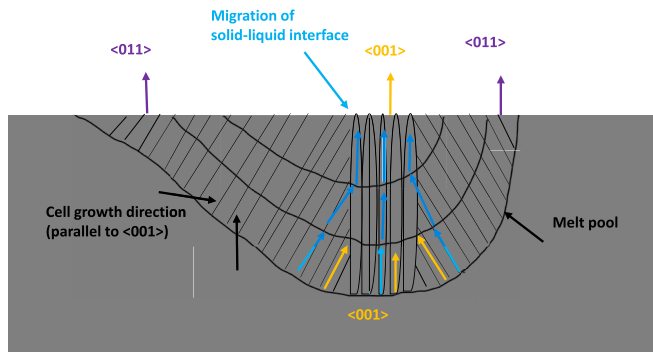


Fig. 2. Original schematic of melt pool boundary, thermal phenomena and columnar grain development occurring during LMD process.



**Fig. 5.** Development of crystal orientation  $\langle 001 \rangle$  in build direction of FeSi 6.5 wt% deposited by LMD process.

### 3.2. Effect of laser power on $\langle 001 \rangle$ texture development

FeSi 6.5 wt% electrical steel was manufactured using LMD, and EBSD was conducted on the XY plane ( $X$  = build direction, BD;  $Y$  = normal direction, ND) to analyse crystallographic texture in the BD-TD plane. EBSD maps of samples TW1 (P: 400 W, V: 400 mm/s, E: 60 J/mm<sup>2</sup>), TW2 (P: 465 W, V: 400 mm/s, E: 69.75 J/mm<sup>2</sup>), and TW3 (P: 500 W, V: 400 mm/s, E: 75 J/mm<sup>2</sup>), shown in Fig. 6 (a–c), confirm a predominant  $\langle 001 \rangle$  fibre-texture along the BD, accompanied by columnar grain growth. This texture strengthens with increasing laser energy density, as evidenced by the larger proportion of red-coloured grains (indicating  $\langle 001 \rangle$  alignment) in TW2 and TW3 compared to TW1, where fewer grains align closely with BD due to lower energy input.

The observed texture and grain morphology correlate with laser power and energy density. At 400 W (TW1), smaller melt pools and faster solidification yield a weaker  $\langle 001 \rangle$  fibre-texture with finer columnar grains. As laser power increases to 465 W (TW2) and 500 W (TW3), larger melt pools and partial remelting of grains enhance epitaxial growth along the BD, where newly solidified material aligns with the  $\langle 001 \rangle$  orientation of prior layers. This aligns with prior studies on direct energy deposition (e.g., LPBF), which note a shift from  $\langle 001 \rangle$  fibre-texture to cube-texture with increasing energy density due to enlarged melt pools [7,38,39]. However, heat transport dynamics further refine this interpretation. As noted in [40] columnar grain growth in non-oriented electrical steels (NGOES) is driven by strong temperature gradients across the material thickness during recrystallization. This phenomenon is particularly relevant in LMD due to

directional heat dissipation along the BD. Additionally, the higher cooling rate along  $\langle 100 \rangle$  directions—compared to other crystallographic axes—favours dendrite alignment and cube-texture development, particularly evident in TW3's stronger texture intensity [40].

Increasing laser energy density also expands the heat-affected zone (HAZ), altering temperature distribution and thermal gradients [41]. In TW2 and TW3, this leads to elongated columnar grains with axes preferentially along BD, as seen in front-view EBSD maps (Fig. 6 (b–c)), alongside a broader HAZ that intensifies remelting and texture evolution. These factors—epitaxial growth, rapid  $\langle 100 \rangle$  cooling, and HAZ effects—collectively explain the transition from a weaker fibre-texture in TW1 to a pronounced cube-texture in TW3, with larger grains and stronger  $\langle 001 \rangle$  alignment. This suggests that LMD parameters can be tuned to control texture and microstructure in FeSi 6.5 wt%, balancing orientation benefits against potential defects like cracks observed at higher energies [42,43].

The orientation distribution functions (ODFs) of the scanned areas are presented in Fig. 7. While all samples exhibited texture, significant differences were observed among them. Sample TW1, processed at 400 W, exhibits a more diffuse texture with fewer pronounced components. Conversely, TW2, processed at 465 W, and TW3, processed at 500 W, show stronger and more defined cube textures. In the  $\varphi_2 = 0^\circ$  section, TW2 and TW3 display a transition to a strong cube texture with increasing laser energy from 400 W to 500 W, particularly near the  $90^\circ$  rotated Goss texture components (011)[0 $\bar{1}$ 1] and Goss texture (110)[100]. This transition is beneficial for the magnetic properties of electrical steel, as cube textures improve magnetic performance. The  $\varphi_2 = 45^\circ$  section further illustrates those components close to (113)[ $\bar{1}$ 2 $\bar{1}$ ] and Goss (110)[001] in TW2 and TW3 also transition into a strong cube texture (001)[100].

Regarding the evolution of  $\{110\}$  orientations, such as the Goss texture (110)[001], their presence is prominent in TW1 ( $\varphi_2 = 45^\circ$ ) and to a lesser extent in TW2 ( $\varphi_2 = 45^\circ$ , (110)[001]) due to smaller melt pools and rapid solidification rates, which restrict extensive recrystallisation or grain reorientation compared to TW3. As laser power increases from 400 W (TW1) to 465 W (TW2) and 500 W (TW3), the  $\{110\}$  orientations diminish gradually, giving way to a dominant cube texture (001)[100]. This shift is driven by enhanced epitaxial growth and steeper thermal gradients at higher energy densities [44], which favour  $\langle 001 \rangle$  alignment over  $\{110\}$  planes as well as formation of large columnar grains [45]. In TW2 ( $\varphi_2 = 0^\circ$ ), traces of  $\{110\}$  persist, including the Goss (011)[100], possibly  $90^\circ$  rotated Goss (011)[ $\bar{0}$ 11] and indicating partial preservation due to localised solidification conditions and incomplete stress relaxation. The role of internal stresses is pivotal in this texture evolution during LMD, rapid cooling in TW1 generates significant thermal stresses from thermal contraction and phase transformation, locking in  $\{110\}$  orientations by limiting grain boundary mobility. In contrast, for TW2 and TW3, higher energy densities (69.75–75 J/mm<sup>2</sup>) reduce cooling rates, expand the HAZ leads to better heat distribution, and facilitate stress relaxation through remelting and recrystallisation, promoting a shift to  $\langle 001 \rangle$  – dominated textures. Thus, internal stresses act as a competing factor—initially stabilising  $\{110\}$  in TW1 but yielding to  $\langle 001 \rangle$  as stress relaxation and grain growth dominate at higher powers.

Notably, almost all samples lack  $\langle 111 \rangle$ //BD ( $\gamma$ -fibre) or  $\langle 110 \rangle$ //RD ( $\alpha$ -fibre) orientations, which are detrimental to the magnetic properties of electrical steel. This absence indicates a favourable texture for magnetic applications. Comparing all samples together, TW2, and TW3 exhibit more pronounced and balanced cube textures, suggesting that higher laser power promotes stronger and more beneficial texture components for magnetic properties. Increasing laser energy density (60 to 75 J/mm<sup>2</sup>) in the LMD technique enhances the cube texture of FeSi, improving its magnetic properties. As laser power rises from 400 W to 500 W, the cube texture becomes more defined, significantly boosting the material's performance, particularly in FeSi 6.5 wt%. This cube

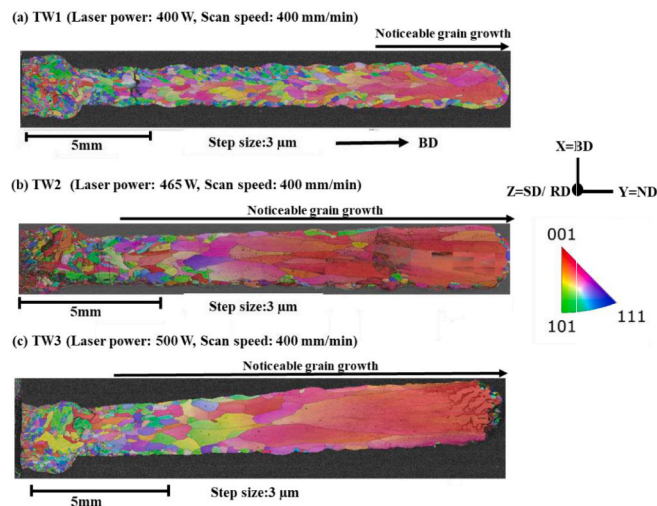


**Fig. 6.** EBSD maps (a, b and c) and IPFs for TW1, TW2 and TW3 in build directions.



the thermal profile and cooling rate, consequently affecting the formation of columnar grains on the side and top planes. This can also lead to an increased depth of the molten pool and a transition from a crystallographic  $\langle 001 \rangle$  fibre texture to a cube texture [7,38]. Thus, laser energy density plays a crucial role in the microstructural evolution, particularly in grain growth during the LMD processes. For example, as can be seen in Fig. 9(a) and (b) provided bar charts compare three samples, TW1, TW2 and TW3, in terms of grain size distribution and the effects of different laser power settings used in their preparation. Sample TW1, prepared with a laser power of 400 W and a scan speed of 400 mm/min, illustrates a grain size distribution predominantly within the 0 to 2000  $\mu\text{m}$  range. Specifically, approximately 71 % (area weighted fraction) of the grains fall within the 0 to 500  $\mu\text{m}$  range, 22 % between 500 and 1000  $\mu\text{m}$ , and 7 % between 1000 and 2000  $\mu\text{m}$ . This indicates a narrow grain size distribution with negligible grains beyond 2000  $\mu\text{m}$ . In contrast, sample TW2, prepared with a higher laser power of 465 W but the same scan speed of 400 mm/min, exhibits a broader and more varied grain size distribution. In TW2, about 26 % of the grains are within the 0 to 500  $\mu\text{m}$  range, 14 % between 500 and 1000  $\mu\text{m}$ , 17 % between 1000 and 2000  $\mu\text{m}$ , and a significant 43 % at the 5000  $\mu\text{m}$  mark. This indicates the presence of much larger grains in TW2 compared to TW1.

Sample TW3, prepared with a laser power of 500 W and a scan speed of 400 mm/min, exhibits a grain size distribution that is more spread out compared to TW1. Notably, the majority of grains are concentrated in two distinct size ranges: 0 to 2000  $\mu\text{m}$  and a significant peak around 4000  $\mu\text{m}$ . Specifically, the data shows that approximately 33 % of the grains are around 4000  $\mu\text{m}$ , indicating a substantial presence of larger grains, while the remainder is mostly within the 0 to 2000  $\mu\text{m}$  range 67 %. This broader distribution, particularly the increase in larger grain sizes, can be attributed to the higher laser power used in TW3, which likely led to slower cooling rates and more extensive grain growth during solidification. This indicates the presence of much larger grains in TW2, TW3 compared to TW1. The comparison highlights that the increase in laser power from 400 W in TW1 to 500 W in TW3 results in a substantial shift in grain size distribution. For example, TW2 shows a reduction in the fraction of smaller grains (0 to 500  $\mu\text{m}$ ) from 71 % to 26 %, a decrease of approximately 63.4 %, and an increase in the proportion of larger grains (5000  $\mu\text{m}$ ) to 43 %, compared to none in TW1. In other words, by increasing the energy density, the grain size increased by 177.78 %. This notable grain growth is also apparent in Fig. 6. These findings highlight the influence of higher laser power on promoting larger grain growth, leading to a broader and coarser grain size distribution in sample TW2 and TW3.

## 4. Conclusion

### 4.1. General overview

The study investigates the microstructure and texture evolution of

FeSi 6.5 wt% electrical steel manufactured using Laser Metal Deposition (LMD), focusing on the impact of varying laser power, scan speed, and energy density. This research highlights the potential of LMD as a versatile technique for tailoring the properties of high-silicon non-grain-oriented electrical steel (NGOES) for advanced applications.

### 4.2. Detailed findings

- **Influence of LMD Parameters:** The LMD process significantly affects microstructure and texture development. Optimisation of laser power and energy density allows precise control over microstructural characteristics.
- **Texture Evolution:** Increasing laser energy density from 60 to 75 J/mm<sup>2</sup> enhances the  $\langle 001 \rangle$  texture along the build direction (BD), with a notable shift toward a cube texture, which is beneficial for magnetic performance in NGOES.
- **Grain Size Correlation:** Higher laser power (400 W to 500 W) increases grain size, favouring the formation of  $\langle 001 \rangle$  texture. This reflects the critical role of thermal gradients and solidification rates in texture evolution.
- **Process Optimisation:** The findings demonstrate that adjusting processing parameters can effectively tailor crystallographic orientations and enhance material properties. Notably, preheating above 200 °C eliminates cracking by reducing thermal gradients, while optimising laser power and energy density further improves microstructural integrity, offering significant opportunities to enhance performance

## 5. Conclusion and further research

These results highlight the capability of LMD to advance the microstructure and texture of high-silicon electrical steel, supporting improved performance in transformers, generators, and electric motors. Moving forward, further research into the electromagnetic properties of this material is planned to fully assess its performance potential. Collaborations with research institutions equipped for such testing are underway, with an aim to present these findings in future publications.

### Research involving human participants and/or animals

This article does not contain any studies involving animals performed and any studies involving human participants performed by any of the authors.

### CRediT authorship contribution statement

**Rasoul Karami:** Writing – review & editing, Writing – original draft, Visualization, Validation, Supervision, Software, Project administration, Methodology, Investigation, Formal analysis, Conceptualization. **David**

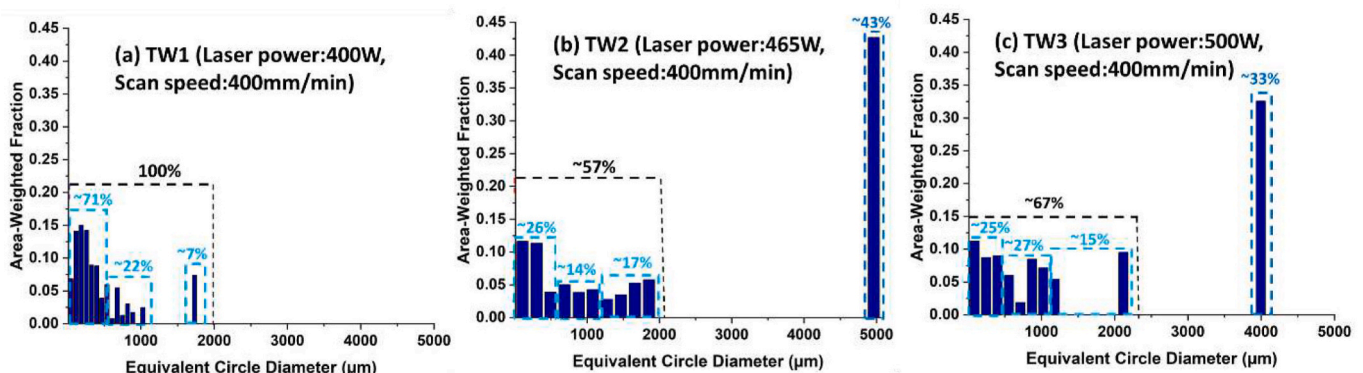


Fig. 9. Grain development based on area weighted fraction of different samples TW1 (a), TW2 (b), TW3 (c).

**Butler:** Writing – review & editing, Visualization, Supervision, Funding acquisition. **Yashar Javadi:** Supervision, Conceptualization. **Saeed Tamimi:** Writing – review & editing, Visualization, Validation, Supervision, Funding acquisition.

## Funding

The authors declare that no funds, grants, or other support were received during the preparation of this manuscript.

## Declaration of competing interest

The authors have no competing interests to declare that are relevant to the content of this article.

All authors certify that they have no affiliations with or involvement in any organization or entity with any financial interest or non-financial interest in the subject matter or materials discussed in this manuscript.

## Data availability

No data was used for the research described in the article.

## References

- R. Karami, D. Butler, S. Tamimi, Manufacturing of non-grain-oriented electrical steels: review, *Int. J. Adv. Manuf. Technol.* (2024), <https://doi.org/10.1007/s00170-024-13837-9>.
- P. Beckley, G.K. Sujan, Steels, silicon iron-based: magnetic properties, in: *Reference Module in Materials Science and Materials Engineering*, Elsevier, 2016.
- C. Li, G. Cai, B. Cai, Q. Wang, Impact of rolling temperature on microstructure, ordered phases, and ductility in Fe–6.5 wt% Si magnetic material, *J. Mater. Res.* 31 (19) (2016) 3004–3015.
- R. Karami, D. Butler, Y. Javadi, S. Tamimi, Process window for manufacturing soft magnetic FeSi 6.5% by laser metal deposition, in: *MATEC Web of Conferences vol. 401*, EDP Sciences, 2024, p. 02011.
- R. Karami, G. Berjokzina, 3D printing, 2022.
- G. Berjokzina, R. Karami, 3D printing in tourism: an answer to sustainability challenges? *Worldwide Hosp. Tourism Themes* 13 (6) (2021) 773–788.
- M. Garibaldi, I. Ashcroft, M. Simonelli, R. Hague, Metallurgy of high-silicon steel parts produced using selective laser melting, *Acta Mater.* 110 (2016) 207–216, <https://doi.org/10.1016/j.actamat.2016.03.037>.
- C. Backes, M. Kahlert, M. Vollmer, M. Smaga, T. Niendorf, T. Beck, Microstructure and magnetic domain structure of additively manufactured Fe–Si soft magnetic alloys with 3 and 9 wt.-% Si, *J. Mater. Res. Technol.* 29 (2024) 1691–1702, <https://doi.org/10.1016/j.jmrt.2024.01.229>.
- H. Williams, Magnetic properties of single crystals of silicon iron, *Phys. Rev.* 52 (7) (1937) 747.
- Y. Hayakawa, *Electrical Steels*, 2020.
- S. Tamimi, et al., Mechanical properties and crystallographic texture of non-oriented electrical steel processed by repetitive bending under tension, *Mater. Sci. Eng. A* 835 (2022) 142665, <https://doi.org/10.1016/j.msea.2022.142665>.
- M. Shiozaki, Y. Kurosaki, The effects of grain size on the magnetic properties of nonoriented electrical steel sheets, *J. Mater. Eng.* 11 (1) (1989) 37–43.
- A.B. Kustas, S. Chandrasekar, K.P. Trumble, Magnetic properties characterization of shear-textured 4 wt% Si electrical steel sheet, *J. Mater. Res.* 31 (24) (2016) 3930–3938.
- H. Pan, Z. Zhang, J. Xie, The effects of recrystallization texture and grain size on magnetic properties of 6.5wt% Si electrical steel, *J. Magn. Magn. Mater.* 401 (2016) 625–632, <https://doi.org/10.1016/j.jmmm.2015.10.047>.
- J.J. Sidor, K. Verbeken, E. Gomes, J. Schneider, P.R. Calvillo, L.A.I. Kestens, Through process texture evolution and magnetic properties of high Si non-oriented electrical steels, *Mater. Charact.* 71 (2012) 49–57, <https://doi.org/10.1016/j.matchar.2012.06.006>.
- A.D. Goodall, J. Uramowski, C.W. Sinclair, L. Chechik, I. Todd, Mechanical properties of stochastically cracked soft magnetic material, *Add. Manuf. Lett.* 7 (2023) 100179, <https://doi.org/10.1016/j.addlet.2023.100179>.
- A. Moses, *Electrical steels: past, present and future developments*, *IEE Proc. A* 137 (5) (1990) 233–245.
- N.A. Spaldin, *Magnetic Materials: Fundamentals and Applications*, Cambridge University Press, 2010.
- J. Creighton, P. Ho, Introduction to chemical vapor deposition (CVD), in: *ASM International vol. 407*, 2001.
- H. Hajji, K. Okada, T. Hiratani, M. Abe, M. Ninomiya, Magnetic properties and workability of 6.5% Si steel sheet, *J. Magn. Magn. Mater.* 160 (1996) 109–114, [https://doi.org/10.1016/0304-8853\(96\)00128-X](https://doi.org/10.1016/0304-8853(96)00128-X).
- K.M. Lee, S.Y. Park, M.Y. Huh, J.S. Kim, O. Engler, Effect of texture and grain size on magnetic flux density and core loss in non-oriented electrical steel containing 3.15% Si, *J. Magn. Magn. Mater.* 354 (2014) 324–332, <https://doi.org/10.1016/j.jmmm.2013.11.030>.
- V.M. Paltanea, G. Paltanea, H. Gavrilă, L. Dumitru, Experimental analysis of magnetic anisotropy in silicon iron steels using the single strip tester, in: *2015 9th International Symposium on Advanced Topics in Electrical Engineering (ATEE)*, IEEE, 2015, pp. 456–459.
- G. Stornelli, et al., Properties of additively manufactured electric steel powder cores with increased Si content, *Materials* 14 (6) (2021) 1489.
- M. Freund, V. Ventzke, F. Dorn, N. Kashaev, B. Klusemann, J. Enz, Microstructure by design: an approach of grain refinement and isotropy improvement in multi-layer wire-based laser metal deposition, *Mater. Sci. Eng. A* 772 (2020) 138635, <https://doi.org/10.1016/j.msea.2019.138635>.
- C. Selcuk, Laser metal deposition for powder metallurgy parts, *Powder Metall.* 54 (2) (2011) 94–99.
- R.W. Fonda, D.J. Rowenhorst, Crystallographic variability in additive manufacturing, in: *IOP Conference Series: Materials Science and Engineering vol. 1249*, IOP Publishing, 2022, p. 012007.
- J.-T. Park, J.A. Szpunar, Effect of initial grain size on texture evolution and magnetic properties in nonoriented electrical steels, *J. Magn. Magn. Mater.* 321 (13) (2009) 1928–1932, <https://doi.org/10.1016/j.jmmm.2008.12.015>.
- J. Li, L. Cao, J. Xu, S. Wang, Q. Zhou, In situ porosity intelligent classification of selective laser melting based on coaxial monitoring and image processing, *Measurement* 187 (2022) 110232, <https://doi.org/10.1016/j.measurement.2021.110232>.
- P. Akbari, et al., MeltPoolNet: melt pool characteristic prediction in metal additive manufacturing using machine learning, *Add. Manuf.* 55 (2022) 102817, <https://doi.org/10.1016/j.addma.2022.102817>.
- J. Wang, R. Zhu, Y. Liu, L. Zhang, Understanding melt pool characteristics in laser powder bed fusion: an overview of single- and multi-track melt pools for process optimization, *Adv. Powder Mater.* 2 (4) (2023) 100137, <https://doi.org/10.1016/j.apmate.2023.100137>.
- S. Ocylok, E. Alexeev, S. Mann, A. Weisheit, K. Wissenbach, I. Kelbassa, Correlations of melt Pool geometry and process parameters during laser metal deposition by coaxial process monitoring, *Phys. Procedia* 56 (2014) 228–238, <https://doi.org/10.1016/j.phpro.2014.08.167>.
- Q. Chen, et al., Elucidating the effect of preheating temperature on melt pool morphology variation in Inconel 718 laser powder bed fusion via simulation and experiment, *Add. Manuf.* 37 (2021) 101642, <https://doi.org/10.1016/j.addma.2020.101642>.
- Y. Zhu, X. Tian, J. Li, H. Wang, Microstructure evolution and layer bands of laser melting deposition Ti–6.5 Al–3.5 Mo–1.5 Zr–0.3 Si titanium alloy, *J. Alloys Compd.* 616 (2014) 468–474.
- A. Ho, H. Zhao, J.W. Fellowes, F. Martina, A.E. Davis, P.B. Prangnell, On the origin of microstructural banding in Ti-6Al4V wire-arc based high deposition rate additive manufacturing, *Acta Mater.* 166 (2019) 306–323, <https://doi.org/10.1016/j.actamat.2018.12.038>.
- T. DebRoy, et al., Additive manufacturing of metallic components—process, structure and properties, *Prog. Mater. Sci.* 92 (2018) 112–224.
- S.S. Sundarram, W. Li, The effect of pore size and porosity on thermal management performance of phase change material infiltrated microcellular metal foams, *Appl. Therm. Eng.* 64 (1) (2014) 147–154, <https://doi.org/10.1016/j.applthermaleng.2013.11.072>.
- S. Kou, *Welding Metallurgy*, New Jersey, USA 431 (446) (2003) 223–225.
- M. Garibaldi, I. Ashcroft, N. Hillier, S.A.C. Harmon, R. Hague, Relationship between laser energy input, microstructures and magnetic properties of selective laser melted Fe-6.9wt Si soft magnets, *Mater. Charact.* 143 (2018) 144–151, <https://doi.org/10.1016/j.matchar.2018.01.016>.
- T. Niendorf, S. Leuders, A. Riemer, H.A. Richard, T. Tröster, D. Schwarze, Highly anisotropic steel processed by selective laser melting, *Metall. Mater. Trans. B Process Metall. Mater. Process. Sci.* 44 (2013) 794–796.
- Y. Sidor, F. Kovac, T. Kvackaj, Grain growth phenomena and heat transport in non-oriented electrical steels, *Acta Mater.* 55 (5) (2007) 1711–1722, <https://doi.org/10.1016/j.actamat.2006.10.032>.
- J. Hijam, R. Balhara, M. Vadali, Investigating double-scan strategies for reducing heat-affected zone in laser surface melting, *Opt. Laser Technol.* 170 (2024) 110289, <https://doi.org/10.1016/j.optlastec.2023.110289>.
- J. Li, H. Ren, C. Liu, S. Shang, The effect of specific energy density on microstructure and corrosion resistance of CoCrMo alloy fabricated by laser metal deposition, *Materials* 12 (8) (2019) 1321.
- X. Shen, F. Meng, K.B. Lau, P. Wang, C.H.T. Lee, Texture and microstructure characterizations of Fe-3.5wt%Si soft magnetic alloy fabricated via laser powder bed fusion, *Mater. Charact.* 189 (2022) 112012, <https://doi.org/10.1016/j.matchar.2022.112012>.
- Y. Liu, J. Shi, Epitaxial growth and stray grain control toward single-crystal metallic materials by additive manufacturing: a review, *Adv. Eng. Mater.* 25 (14) (2023) 2201917.
- P. Ledwig, et al., Tailoring microstructure and mechanical properties of additively manufactured Inconel 625 by Remelting strategy in laser powder bed fusion, *Metall. Mater. Trans. A* 55 (7) (2024) 2485–2508.
- Y. He, E. Hilinski, J. Li, Texture evolution of a non-oriented electrical steel cold rolled at directions different from the hot rolling direction, *Metall. Mater. Trans. A* 46 (2015) 5350–5365.
- Z. Chen, W. Sun, Y. Huang, H. Zhou, K. Yang, J. Lu, The effect of laser energy density on microstructural evolution and mechanical properties of laser clad 316L stainless steel for repair, *Surf. Coat. Technol.* 448 (2022) 128899, <https://doi.org/10.1016/j.surfcoat.2022.128899>.

- [48] Z. Cheng, et al., Balancing magnetic and mechanical properties of non-oriented electrical steel: correlation between microstructure and properties, *Acta Metall. Sin.* (2024), <https://doi.org/10.1007/s40195-024-01757-2>.
- [49] A.R.A. Dezfoli, W.-S. Hwang, W.-C. Huang, T.-W. Tsai, Determination and controlling of grain structure of metals after laser incidence: theoretical approach, *Sci. Rep.* 7 (1) (2017) 41527.
- [50] Z. Lin, et al., Crystallographic Texture Control of Niti Alloy by Adjusting the Thermal Gradient of Laser Powder Bed Melting, 2024. Available at SSRN 4745122.
- [51] M. Sanjari, et al., Microstructure, texture, and anisotropic mechanical behavior of selective laser melted maraging stainless steels, *Mater. Charact.* 192 (2022) 112185, <https://doi.org/10.1016/j.matchar.2022.112185>.
- [52] C. Bernauer, M.E. Sigl, S. Grabmann, T. Merk, A. Zapata, M.F. Zaeh, Effects of the thermal history on the microstructural and the mechanical properties of stainless steel 316L parts produced by wire-based laser metal deposition, *Mater. Sci. Eng. A* 889 (2024) 145862, <https://doi.org/10.1016/j.msea.2023.145862>.
- [53] M.R. Borhani, M. Rajabi, R.S. Razavi, R. Jamaati, Investigating the relationship between mechanical properties and residual stress in the laser cladding process of Inconel 625 superalloy, *Heliyon* 9 (9) (2023).
- [54] X. Zou, Z. Yan, K. Zou, S. Gang Zhang, W. Liu, L. Song, Residual stress control of 316 L stainless steel using pulsed-wave laser additive manufacturing, *Opt. Laser Technol.* 150 (2022) 107910, <https://doi.org/10.1016/j.optlastec.2022.107910>.